

Numerical analyses of M31 dark matter profiles

Kuantay Boshkayev,^{1,2,3*} Talgar Konysbayev,^{1,2†} Yergali Kurmanov,^{1,2‡} Orlando Luongo,^{2,4,5§}
 Marco Muccino,^{2¶} Hernando Quevedo,^{2,6,7||} and Gulnur Zhumakhanova^{8**}

¹National Nanotechnology Laboratory of Open Type, Al-Farabi ave. 71, Almaty, Kazakhstan.

²Al-Farabi Kazakh National University, Al-Farabi ave. 71, Almaty, Kazakhstan.

³Department of Physics, Nazarbayev University, 53 Kabanbay Batyr, Astana, Kazakhstan.

⁴Scuola di Scienze e Tecnologie, Divisione di Fisica, Università di Camerino, Via Madonna delle Carceri 9, Camerino, Italy.

⁵Istituto Nazionale di Fisica Nucleare, Sezione di Perugia, via A. Pascoli, I-06123 Perugia, Italy.

⁶Instituto de Ciencias Nucleares, Universidad Nacional Autónoma de México, Mexico.

⁷Dipartimento di Fisica and ICRA, Università di Roma “La Sapienza”, Roma, Italy.

⁸National Center of Science and Technology Evaluation, 221 Bogenbay batyr, Almaty, Kazakhstan.

7 December 2022

ABSTRACT

We reproduce the rotation curve of the Andromeda galaxy (M31) by taking into account its bulge, disk, and halo components, considering the last one to contain the major part of dark matter mass. Hence, our prescription is to split the galactic bulge into two components, namely, the inner and main bulges, respectively. Both bulges are thus modeled by exponential density profiles since we underline that the widely accepted de Vaucouleurs law fails to reproduce the whole galactic bulge rotation curve. In addition, we adopt various well-known phenomenological dark matter profiles to estimate the dark matter mass in the halo region. Moreover, we apply the least-squares fitting method to determine from the rotation curve the model free parameters, namely, the characteristic (central) density, scale radius, and consequently the total mass. To do so, we perform Markov chain Monte Carlo statistical analyses based on the Metropolis algorithm, maximizing our likelihoods adopting velocity and radii data points of the rotation curves. We do not fit separately the components for bulges, disk and halo, but we perform an overall fit including all the components and employing all the data points. Thus, we critically analyze our corresponding findings and, in particular, we employ the Bayesian Information Criterion to assess the most accredited model to describe M31 dark matter dynamics.

Key words: Spiral galaxies. Dark matter. Rotational curve. Phenomenological profiles.

1 INTRODUCTION

At large distances from the centers, stars within spiral galaxies rotate with anomalous speeds (Banik et al. 2020; Elson 2014), indicating that galaxy rotation curves are fundamental to disclose the unknown nature of *dark matter* (DM). The evidences of large amounts of invisible matter, distributed differently from the stellar and gaseous disks, turned up in the 1970s (Roberts 1978; Faber & Gallagher 1979; Rubin et al. 1980; Bosma 1981). In fact, optical and 21-cm rotation curves (RCs) were found to behave in an anomalous way, fully-incompatible with the Keplerian fall-off predicted from the outer distribution of luminous matter. Hence, the determination of the DM abundance, *i.e.*, of the mass distribution in spiral galaxies, is essential in order to figure out its physical properties. In this regard,

a widely-consolidate technique consists in analyzing rotation curves (Sofue 2009; Salucci 2019a; Dehghani et al. 2020).

Furthermore, the corresponding DM gravity field keeps galaxies and cluster of galaxies stable, being essential to describe perturbations regimes in cosmology too (Bernardeau et al. 2002). Confirmations of the DM existence are numerous and come from several observational evidences, *e.g.*, in galaxy clusters, hot gas motion, gravitational microlensing (Nakama 2020), and clustering of structures (Event Horizon Telescope Collaboration et al. 2019).

However, the DM nature is still highly-debated since no suitable candidates as DM particles have been experimentally found. In particular, the existence of DM appears evident through dynamical measurements, but not with interaction with ordinary matter or radiation, providing that no ground-based laboratories have been able to detect DM particles yet (Woithe & Kersting 2021). Consequently, the DM nature is still challenging and unknown (Herrera & Ibarra 2021). In this respect, a widely-accepted hypothesis is that DM consists of a class of weakly interacting massive particles and/or of (ultra-)light

* kuantay@mail.ru

† talgar_777@mail.ru

‡ kurmanov.yergali@kaznu.kz

§ orlando.luongo@unicam.it

¶ marco.muccino@lnf.infn.it

|| quevedo@nucleares.unam.mx

** zhumakhanovag@gmail.com

particles, although alternative viewpoints have been proposed¹, see e.g. (Bertone & Hooper 2018) and references therein².

In addition, at zeroth approximation *different* phenomenological density profiles are adopted to explain the observed rotation curves in galaxies. For instance, for the Milky Way (MW) galaxy, different DM profiles are used to obtain information about the RCs from the central part of the galaxy to the halo (Boshkayev et al. 2021).

In this work, motivated by the fact that detailed RC outcomes have been investigated in the Andromeda galaxy (Corbelli et al. 2010; Carignan et al. 2006; Rubin & Ford 1970), and are used for the distribution of masses in the disk and the dark halo, we analyze the M31 RCs and consider all the possible morphological configurations of the galaxy itself. In particular, we focus on both inner and main bulge regions, on the disk and finally on the halo component, considered as the main target whose phenomenological profile, among the consolidate profiles, is preferable from a statistical standpoint. To this end, we work out six profiles, i.e., the *exponential sphere* (hereafter *ES*), *pseudo-isothermal* (hereafter *ISO*), *Burkert*, *Navarro-Frenk-White* (NFW), *Moore*, *Beta* and the *Brownstein profile* and we estimate the corresponding DM abundance in each component of the galaxy. Afterwards, we follow the subsequent steps:

- analysis of the RC data of M31,
- determination of the model free parameters from the log-likelihood approach and, finally,
- reconstruction of the theoretical RC of M31.

The latter step is attained by using the data from Sofue (2015) and carrying out a similar analysis that differs by the following aspects:

- we divide the bulge into *inner* and *main bulges*. A similar analysis has been performed for the MW (see e.g., Sofue 2013), where the RC is better described in terms of two bulges, and by analogy can be applied to M31 since two distinct bumps below 4 kpc are clearly visible in the RC³;
- we adopt the exponential density profile for inner and main bulges in analogy to Sofue (2013) and Boshkayev et al. (2021).
- we consider alternative profiles for the halo and determine the most suitable from the statistical point of view.

In this respect, we extend the analysis performed in Sofue (2015), where the RC has been constructed for a bulge, a disk and a dark halo, employing only the NFW profile for the halo. Remarkably, we demonstrate that the NFW is not the most accredited profile under the above hypotheses. Further, we compare our findings with the MW, emphasizing the main physical differences.

¹ Geometric DM has been formulated in the context of extended theories of gravity, e.g., Capozziello et al. (2019), DM quasi-particles in Belfiglio et al. (2022) and/or unified dark sector models (Boshkayev et al. 2019), modifications of the Newton law in Milgrom (2020), and so on.

² Possible scenarios that minimally extend the standard model of particle physics would predict axions, gravitinos, etc., see e.g. Bertone et al. (2005); Salucci (2019b); Quiskamp et al. (2022); Marrodán Undagoitia et al. (2022). Other alternatives involve highly-massive structures, such as MACHOS, see e.g. Brandt (2016); Chapline & Frampton (2016); Bai et al. (2020); Katz et al. (2020); Yang (2022), or modifications of gravity at large scales due to extra terms, see e.g. Capozziello et al. (2019).

³ The bulge structure greatly varies with the type of galaxies. For example, elliptical galaxies consist only of a spherical bulge, whereas irregular ones have a weak bulge. Most of the RCS of the galaxies considered by Bernal et al. (2018) exhibits only one bulge. However, some galaxies may have a less evident second bulge. Indeed, according to Beaton et al. (2007), Mould (2013) and Blańa Díaz et al. (2017) M31 has two bulges.

The paper is organized as follows. In Section 2, we review well-known phenomenological DM profiles. In Section 3, we introduce the basic ideas and hypotheses of the work and present the results of fitting RC data for M31 and MW galaxies. In Section 5, we briefly discuss our outcomes and compare them with other known results. Finally, we summarize the main conclusions of our work.

2 PHENOMENOLOGICAL DARK MATTER PROFILES

Bulge and disk mainly consist of baryonic (visible) matter, with the bulge mostly composed of older stars and the disk composed of star forming regions, gas and dust.

Galactic halos are assumed to be composed of DM only. Their density profiles can be obtained by using numerical simulation methods of stars dynamics in galaxies. Here, we selected the most adopted ones, namely ISO, Beta, Burkert, Brownstein, Moore, NFW and ES. All these profiles are characterized by two parameters: the characteristic central density of DM ρ_0 and the scale radius r_0 , that can be expressed as functions of the dimensionless distance $x = x(r) = r/r_0$. The above models, split into:

Cored profiles.

1. ISO (Jimenez et al. 2003)

$$\rho_{ISO}(x) = \frac{\rho_0}{1 + x^2}; \quad (1)$$

2. Burkert (Burkert 1995)

$$\rho_{Bur}(x) = \frac{\rho_0}{(1+x)(1+x^2)}; \quad (2)$$

3. Beta with $\beta = 1$ (Navarro et al. 1995; Sofue 2020)

$$\rho_{Beta}(x) = \frac{\rho_0}{(1+x^2)^{1.5}}; \quad (3)$$

4. Brownstein (Brownstein & Moffat 2006; Sofue 2020)

$$\rho_{Bro}(x) = \frac{\rho_0}{1+x^3}. \quad (4)$$

Cuspy profiles.

5. NFW (Navarro et al. 1996), based on cosmological models of halo formation,

$$\rho_{NFW}(x) = \frac{\rho_0}{x(1+x)^2}; \quad (5)$$

6. Moore (Moore et al. 1998)

$$\rho_{Moore}(x) = \frac{\rho_0}{x^{1.16}(1+x)^{1.84}}. \quad (6)$$

The distinction between cored and cuspy models concerns the cusp of density as $r \rightarrow 0$ for the latter two approaches and the smoothness of the first four models in the same regime.

Figure 1 shows the dependence of ρ/ρ_0 on r/r_0 for the DM phenomenological profiles. In this dimensionless representation, one can see that the profiles differ from each other at small and large distances, as for each profile one can have different values of ρ_0 and r_0 . Any profile generates a distinct RC and hence yields corresponding DM mass distributions that can be calculated as

$$M_h(r) = \int_0^r 4\pi x^2 \rho(x) dx, \quad (7)$$

where $\rho(x)$ is any of the DM profiles from Eqs. (1)–(6).

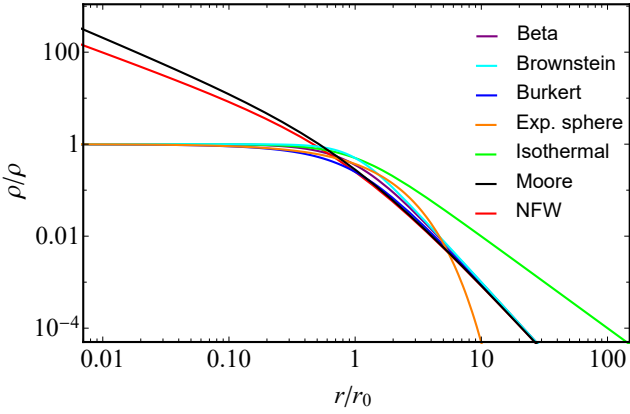


Figure 1. Comparison among phenomenological DM density profiles. Here, ρ_0 is not fixed since we plot the normalised density ρ/ρ_0 .

2.1 Inner parts of M31

Inner parts of galaxies are usually modeled by the de Vaucouleurs profile defining the surface mass density

$$\Sigma_b(x) = \Sigma_{bc} \exp \left[\kappa \left(1 - x^{1/4} \right) \right], \quad (8)$$

where $\kappa = 7.6695$, $x = r/r_b$, Σ_{bc} is the central value of the surface mass density, and r_b is the scale radius of the bulge. The total mass of the bulge is given by

$$M_{bt} = 2\pi \int_0^\infty \Sigma_b(r) r dr = \eta r_b^2 \Sigma_{bc}, \quad (9)$$

where $\eta = 22.665$ is a dimensionless constant. The mass enclosed within a sphere of radius r is given by

$$M_{bt}(r) = 4\pi \int_0^r \rho_b(y) y^2 dy, \quad (10)$$

where the volume density $\rho_b(y)$ is calculated as

$$\rho_b(y) = \frac{1}{\pi} \int_y^\infty \frac{d\Sigma_b(x)}{dx} \frac{dx}{\sqrt{x^2 - y^2}}. \quad (11)$$

It was shown that the de Vaucouleurs law fails to fit the bulge RC of the MW galaxy. As an alternative in Sofue (2013) the bulge was split into inner and main bulges, both modeled by ES profiles

$$\rho(x) = \rho_0 \exp(-x), \quad (12)$$

where $x = r/r_0$. The mass enclosed within a sphere of radius r reads

$$M(r) = M_0 \left[1 - \exp(-x) \left(1 + x + x^2/2 \right) \right], \quad (13)$$

where the total mass M_0 is given by

$$M_0 = 4\pi \int_0^\infty r^2 \rho(r) dr = 8\pi r_0^3 \rho_0. \quad (14)$$

Later in the text, we show that inner and main bulges modeled by two profiles as in Eq. (12) are statistically and visually better than the case modeled by one bulge only, adopting Eq. (8). In addition to this prescription, we underline that Eq. (8) represents a surface density, whereas Eq. (12) consists of a volume density and, consequently, we cannot compare the two profiles to each other.

2.2 The galactic disk

The galactic disk is usually represented by an exponential disk with a surface mass density (Freeman 1970)

$$\Sigma_d(x) = \Sigma_{dc} \exp(-x), \quad (15)$$

where $x = r/r_d$, Σ_{dc} is the central value of the surface density and r_d is the disk scale radius. The mass enclosed within a radius r is

$$M_d(r) = M_{dt} \left[1 - \exp(-x) (1 + x) \right], \quad (16)$$

where the total mass is M_{dt} is given by

$$M_{dt} = 2\pi \int_0^\infty \Sigma_d(r) r dr = 2\pi r_d^2 \Sigma_{dc}. \quad (17)$$

The rotation curve for a thin exponential disk is given by (Binney & Tremaine 1987).

$$V_d(y) = \sqrt{\frac{2GM_{dt}}{r_d} y^2 [I_0(y)K_0(y) - I_1(y)K_1(y)]}, \quad (18)$$

where $y = r/(2r_d)$, and I_i and K_i are the modified Bessel functions of the first and second kind, respectively.

3 INFERENCE OF THE MODEL PARAMETERS AND DARK MATTER MASS

The linear velocity V of stars and gas depends upon the galactocentric distance r and it is determined by equating the centripetal and gravitational forces (via the internal gravitational potential Φ) acting on a star moving in a circular orbit

$$V(r) = \sqrt{\frac{GM(r)}{r}} = \sqrt{r \frac{\partial \Phi(r)}{\partial r}}, \quad (19)$$

where G is the gravitational constant.

Now, we can fit the RC of M31 to extract the model free parameters. We here consider the case with one bulge, disk and halo, in analogy with Sofue (2015), and the case with the splitting of the bulge into inner and main components, in agreement with Sofue (2013). In the latter case, the resulting RC is given by

$$V(r)^2 = V_{ib}(r)^2 + V_{mb}(r)^2 + V_d(r)^2 + V_h(r)^2, \quad (20)$$

where V_{ib} , V_{mb} , V_d and V_h are the linear velocities of test particles (stars) in the gravitational field of the mass distribution at distance r of inner and main bulges, disk, and halo, respectively.

We modified the Wolfram Mathematica code from Arjona et al. (2019) and performed Markov chain – Monte Carlo fits of the RC of Andromeda, by means of the Metropolis algorithm, searching for the best-fit parameters maximizing the log-likelihood

$$\ln \mathcal{L} = -\frac{1}{2} \sum_{k=1}^N \left\{ \left[\frac{V_k - V(r_k)}{\sigma V_k} \right]^2 + \ln(2\pi \sigma V_k^2) \right\}, \quad (21)$$

where $N = 46$ are the velocity data points V_k at radii r_k of the RC and σV_k are the attached errors. We first reproduced the results of Sofue (2015) and then inferred the model free parameters using Eq. (20). Differently from Sofue (2013, 2015), we do not split the RC and fit separately the components for bulge(s), disk and halo, but we perform an overall fit including all the components and employing all the data points without splitting them.

To assess the best-fit model out of the six profiles when considering the halo, we used the Bayesian Information Criterion (BIC)

$$\text{BIC} = -2 \ln \mathcal{L}_{\max} + k \ln N, \quad (22)$$

where k is the number of model parameters and \mathcal{L}_{\max} the maximum value of the log-likelihood (Yunis et al. 2020). In general, the model with the lowest BIC test, say BIC_0 , is considered to be the reference (best-suited) model. The statistical evidence in support of the reference model to the best-fitting one, when compared to other

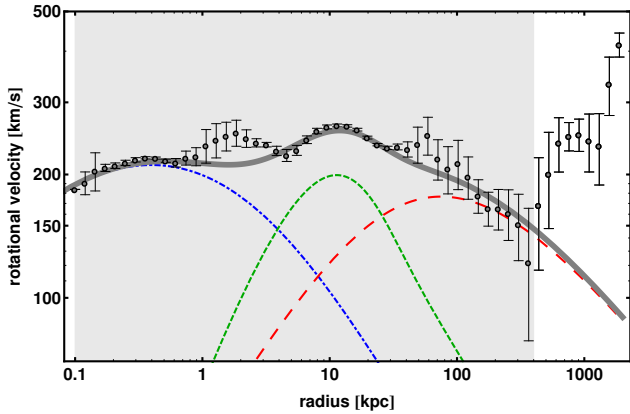


Figure 2. Best-fit RC of M31 (thick, gray) composed of bulge (de Vaucouleurs, dot-dashed blue), disk (Freeman, dashed green) and halo (NFW, long-dashed red) components. The shaded area marks the data (black dots with error bars) considered for the fitting. Reproduced from Sofue (2015).

Table 1. The best-fit parameters of M31 from Sofue (2015). The halo model is the NFW profile and its mass was calculated within $r = 200$ kpc.

| Parts | Total mass ($10^{11} M_{\odot}$) | Scale radius (kpc) | Central density ($10^{-3} M_{\odot}/\text{pc}^3$) |
|-------|---------------------------------------|-----------------------|--|
| Bulge | 0.35 ± 0.004 | 1.35 ± 0.02 | — |
| Disk | 1.26 ± 0.08 | 5.28 ± 0.25 | — |
| Halo | 12.30 ± 2.60 | 34.60 ± 2.10 | 2.23 ± 0.24 |

models, is certified by the difference $\Delta\text{BIC} = \text{BIC} - \text{BIC}_0$ and, in particular, by:

1. $\Delta\text{BIC} \in [0, 2]$ showing a weak evidence.
2. $\Delta\text{BIC} \in (2, 6]$ showing a mild evidence.
3. $\Delta\text{BIC} > 6$ showing a huge evidence.

4 THEORETICAL RESULTS

Fig. 2 and Tables 1 reproduce the results of the RC analysis of M31 obtained by Sofue (2015). The bulge is modelled by the de Vaucouleurs profile (de Vaucouleurs 1958), the disk is approximated by the exponential disk model (Freeman 1970) and the halo was described by the NFW model (Navarro et al. 1996). The fitting was performed within the range 0–20 kpc for the bulge, 0–40 kpc for the disk, and 0–385 kpc for the halo (Sofue 2015).

Table 2 lists the best-fit results obtained from the ~ 0 –400 kpc RC by considering a single bulge Sofue (2015). We fixed the de Vaucouleurs profile for the bulge, the Freeman profile for the disk, whereas for the halo we explored the profiles in Eqs. (1)–(6) and the ES profile. This comparison among all the DM halo profiles allows us to perform better and objective analyses. The last combination of models listed in Table 2 represents a direct comparison, though performed with a different methodology (see Sec. 3), with the results of Sofue (2015) summarized Table 1. As one can see, the NFW profile is not the most preferred model according to ΔBIC .

Table 3 lists the best-fit results obtained from the ~ 0 –400 kpc RC data by splitting the bulge into inner and main components in analogy to Sofue (2013). We fixed the exponential sphere density profile for both inner and main bulges and the Freeman density profile for the disk, whereas for the halo we explored all the DM density profiles in Eqs. (1)–(6) and the exponential sphere profile.

To compare the results of Tables 2–3, we computed the difference ΔBIC with respect to the model providing the lowest value BIC_0 . According to this test, it turned out that the models with ES density profiles for both inner and main bulges indeed fit better than the de Vaucouleurs profile for a single bulge, with the latter models providing $\Delta\text{BIC} \gtrsim 12$ –20 with respect to the former ones. In particular, in Table 3 we see that the best-fit model with the lowest value $\text{BIC}_0 = 224.35$ is the two-bulge model with a DM halo described by the ES density profile; also the Brownstein profile represents a good fit for the DM halo, being $\Delta\text{BIC} \approx 2$. The NFW profile, like the Moore profile, does not perform well, since $\Delta\text{BIC} \approx 11$. In absolute, the worst fit is given by the ISO profile with $\Delta\text{BIC} \approx 20$; this is also certified by the fact that the RC of M31 is not flat in the halo region (see Sofue 2015, for details).

Also in the case of fits with a single bulge described by the de Vaucouleurs profile (strongly excluded with respect to the fits with two bulges), among the considered DM density profiles, ES profile ($\Delta\text{BIC} \approx 18$) and Brownstein profile ($\Delta\text{BIC} \approx 19$) fit better than NFW and Moore profiles ($\Delta\text{BIC} \approx 24$), whereas the ISO profile ($\Delta\text{BIC} \approx 40$) is definitely the worst-performing one (see Table 2).

We performed also more conservative approaches involving two de Vaucouleurs profiles for inner and main bulges. However, we obtained higher BIC and ΔBIC values (not reported here for the sake of clarity and simplicity of the presentation), certifying that two ES profiles provide better a fit.

The RC data with error bars of the M31 galaxy is illustrated in the left panel of Fig. 3. Superposed on the observational data, the best-fit curves are also displayed: the inner and main bulges modeled with two exponential density profiles, the disk with the Freeman profile, and the halo region with the exponential density model (see values in Table 3). On the right panel of Fig. 3, we focused on the halo sector of the RC of M31, showing all the DM profiles considered in this work. It is worth noticing that, unlike DM profiles for halos, there are not so many alternatives for the inner parts of galaxies.

Fig. 4 displays the density $\rho(r)$ (top left panel), the mass $M(r)$ (top right panel), the pressure $P(r)$ (bottom left panel) and the speed of sound $c_s = \sqrt{\partial P / \partial \rho}$ (bottom right panel) radial distributions obtained from the combination of models that best-fit inner bulge, main bulge, disk and DM halo of M31 (see Table 3). As expected the main contribution to the mass of the galaxy is given by the presence of DM in the halo. Following Barranco et al. (2015), the pressure in the whole galaxy was assumed to be non-zero and has been estimated from the Newtonian hydrostatic equilibrium equations

$$\frac{dM(r)}{dr} = 4\pi r^2 \rho(r), \quad (23a)$$

$$\frac{dP(r)}{dr} = -\rho(r) \frac{GM(r)}{r^2}. \quad (23b)$$

The speed of sound, obtained from the hydrostatic equilibrium equation, is given by the expression

$$c_s(r) = V(r) \sqrt{-\frac{d \ln r}{d \ln \rho(r)}}, \quad (24)$$

from which it is clear its correlation with the RC velocity.

4.1 Comparison with the Milky Way galaxy

The MW is a spiral galaxy with a structure similar to M31 and so it appears natural and needful a direct comparison between the two galaxies. The RC data of the MW has been updated in Sofue (2015), taking into account the linear speed of the Sun with respect to the

Table 2. Best-fit RC parameters of M31 obtained by considering one bulge (de Vaucouleurs), disk (Freeman) and the halo models considered in this work. The halo mass has been calculated within $r = 200$ kpc. The ΔBIC value is computed with respect to the minimum BIC in Table 3.

| Bulge | | Disk | | Halo | | | ΔBIC |
|--------------------------------|------------------------|--------------------------------|------------------------|---|--------------------------|--------------------------------|--------------------|
| M_b ($10^{11} M_\odot$) | r_b (kpc) | M_d ($10^{11} M_\odot$) | r_d (kpc) | ρ_0 ($10^{-3} M_\odot/\text{pc}^3$) | r_0 (kpc) | M_h ($10^{11} M_\odot$) | |
| de Vaucouleurs | | Freeman | | Beta | | | 21.48 |
| $0.43^{+0.05}_{-0.02}$ | $1.58^{+0.16}_{-0.08}$ | $1.54^{+0.10}_{-0.07}$ | $4.98^{+0.27}_{-0.20}$ | $3.10^{+0.48}_{-0.70}$ | $26.23^{+3.32}_{-2.08}$ | $12.22^{+4.23}_{-3.64}$ | |
| de Vaucouleurs | | Freeman | | Brownstein | | | 19.43 |
| $0.45^{+0.04}_{-0.03}$ | $1.64^{+0.13}_{-0.10}$ | $1.66^{+0.07}_{-0.04}$ | $5.21^{+0.24}_{-0.15}$ | $1.82^{+0.13}_{-0.28}$ | $30.12^{+3.56}_{-1.03}$ | $11.82^{+3.56}_{-2.07}$ | |
| de Vaucouleurs | | Freeman | | Burkert | | | 22.68 |
| $0.43^{+0.05}_{-0.03}$ | $1.56^{+0.17}_{-0.09}$ | $1.45^{+0.09}_{-0.09}$ | $4.87^{+0.21}_{-0.20}$ | $5.37^{+1.14}_{-1.32}$ | $22.93^{+3.62}_{-2.13}$ | $12.16^{+5.30}_{-4.04}$ | |
| de Vaucouleurs | | Freeman | | ES | | | 17.56 |
| $0.45^{+0.05}_{-0.03}$ | $1.62^{+0.15}_{-0.10}$ | $1.59^{+0.06}_{-0.05}$ | $5.11^{+0.20}_{-0.13}$ | $3.40^{+0.39}_{-0.44}$ | $23.10^{+1.85}_{-1.01}$ | $10.45^{+2.75}_{-1.90}$ | |
| de Vaucouleurs | | Freeman | | ISO | | | 40.47 |
| $0.48^{+0.04}_{-0.04}$ | $1.74^{+0.14}_{-0.14}$ | $1.21^{+0.15}_{-0.06}$ | $4.89^{+0.21}_{-0.22}$ | $17.31^{+2.32}_{-7.84}$ | $6.33^{+2.37}_{-0.58}$ | $16.58^{+1.23}_{-8.07}$ | |
| de Vaucouleurs | | Freeman | | Moore | | | 23.85 |
| $0.35^{+0.06}_{-0.02}$ | $1.33^{+0.21}_{-0.07}$ | $1.00^{+0.17}_{-0.08}$ | $4.62^{+0.29}_{-0.14}$ | $3.01^{+1.26}_{-1.54}$ | $29.57^{+11.61}_{-4.39}$ | $12.39^{+1.27}_{-7.71}$ | |
| de Vaucouleurs | | Freeman | | NFW | | | 23.62 |
| $0.39^{+0.04}_{-0.03}$ | $1.45^{+0.14}_{-0.12}$ | $1.08^{+0.11}_{-0.08}$ | $4.65^{+0.27}_{-0.19}$ | $3.68^{+1.72}_{-1.27}$ | $28.28^{+6.85}_{-4.87}$ | $13.62^{+9.38}_{-6.76}$ | |

Table 3. Best-fit RC parameters of M31 obtained by considering inner (ES) and main bulges (ES), disk (Freeman) and the halo models considered in this work. The halo mass has been calculated within $r = 200$ kpc. The ΔBIC value is computed with respect to the model with the ES DM halo.

| Inner Bulge | | Main Bulge | | Disk | | Halo | | | ΔBIC |
|-----------------------------------|---------------------------|-----------------------------------|------------------------|--------------------------------|------------------------|---|-------------------------|--------------------------------|--------------------|
| M_{ib} ($10^{11} M_\odot$) | r_{ib} (kpc) | M_{mb} ($10^{11} M_\odot$) | r_{mb} (kpc) | M_d ($10^{11} M_\odot$) | r_d (kpc) | ρ_0 ($10^{-3} M_\odot/\text{pc}^3$) | r_0 (kpc) | M_h ($10^{11} M_\odot$) | |
| ES | | ES | | Freeman | | Beta | | | 4.99 |
| $0.033^{+0.002}_{-0.002}$ | $0.069^{+0.003}_{-0.003}$ | $0.19^{+0.02}_{-0.01}$ | $0.44^{+0.03}_{-0.02}$ | $1.72^{+0.08}_{-0.07}$ | $5.25^{+0.17}_{-0.15}$ | $2.57^{+0.45}_{-0.47}$ | $28.09^{+3.96}_{-1.85}$ | $13.36^{+5.01}_{-5.58}$ | |
| ES | | ES | | Freeman | | Brownstein | | | 2.07 |
| $0.033^{+0.001}_{-0.001}$ | $0.069^{+0.003}_{-0.001}$ | $0.20^{+0.01}_{-0.01}$ | $0.44^{+0.02}_{-0.01}$ | $1.89^{+0.03}_{-0.09}$ | $5.53^{+0.12}_{-0.21}$ | $1.38^{+0.30}_{-0.07}$ | $33.27^{+1.96}_{-2.68}$ | $11.49^{+3.01}_{-2.35}$ | |
| ES | | ES | | Freeman | | Burkert | | | 7.13 |
| $0.033^{+0.003}_{-0.001}$ | $0.070^{+0.004}_{-0.004}$ | $0.19^{+0.02}_{-0.01}$ | $0.43^{+0.03}_{-0.01}$ | $1.63^{+0.09}_{-0.09}$ | $5.07^{+0.26}_{-0.14}$ | $4.50^{+0.81}_{-1.13}$ | $24.87^{+4.34}_{-1.85}$ | $12.38^{+5.62}_{-3.80}$ | |
| ES | | ES | | Freeman | | ES | | | 0.00 |
| $0.033^{+0.002}_{-0.002}$ | $0.069^{+0.003}_{-0.003}$ | $0.20^{+0.01}_{-0.02}$ | $0.45^{+0.02}_{-0.03}$ | $1.79^{+0.03}_{-0.08}$ | $5.43^{+0.05}_{-0.23}$ | $2.88^{+0.41}_{-0.26}$ | $24.59^{+1.40}_{-1.00}$ | $10.64^{+2.34}_{-1.59}$ | |
| ES | | ES | | Freeman | | ISO | | | 20.17 |
| $0.033^{+0.003}_{-0.001}$ | $0.069^{+0.004}_{-0.002}$ | $0.21^{+0.01}_{-0.01}$ | $0.45^{+0.03}_{-0.01}$ | $1.27^{+0.17}_{-0.05}$ | $5.21^{+0.12}_{-0.33}$ | $36.08^{+12.34}_{-12.34}$ | $4.21^{+3.28}_{-3.28}$ | $15.54^{+23.81}_{-10.22}$ | |
| ES | | ES | | Freeman | | Moore | | | 11.32 |
| $0.033^{+0.001}_{-0.002}$ | $0.070^{+0.001}_{-0.004}$ | $0.19^{+0.01}_{-0.01}$ | $0.44^{+0.01}_{-0.02}$ | $1.30^{+0.10}_{-0.04}$ | $5.01^{+0.15}_{-0.13}$ | $2.54^{+0.47}_{-0.93}$ | $33.05^{+8.40}_{-2.45}$ | $13.59^{+8.54}_{-5.50}$ | |
| ES | | ES | | Freeman | | NFW | | | 11.29 |
| $0.033^{+0.002}_{-0.001}$ | $0.069^{+0.004}_{-0.003}$ | $0.18^{+0.02}_{-0.01}$ | $0.43^{+0.03}_{-0.01}$ | $1.27^{+0.12}_{-0.09}$ | $4.92^{+0.28}_{-0.13}$ | $2.49^{+1.40}_{-0.83}$ | $33.93^{+7.62}_{-6.71}$ | $13.13^{+9.95}_{-7.45}$ | |

galactic center as $V_\odot = 238$ km/s instead of $V_\odot = 200$ km/s (Sofue 2013).

Fig. 5 and Tables 4 reproduce the results of the RC analysis of the MW obtained by Sofue (2015). In analogy to M31, the bulge is modelled by the de Vaucouleurs profile, the disk is approximated by the exponential disk model and the halo was described by the NFW model. The fitting was performed within the range 0–20 kpc for the bulge, 0–40 kpc for the disk, and 0–385 kpc for the halo (Sofue 2015).

The MW RC data and corresponding detailed analyses, invoking the ES density profile for both inner and main bulges, the Freeman model for the disk and the NFW profile for the halo region, have been presented in Sofue (2013). The extension of the analyses by Sofue (2013) was given in Boshkayev et al. (2021), where the ES density profile has also been used to interpret the RC data in the disk and halo of the galaxy along with other widely exploited profiles. However, in Boshkayev et al. (2021) in order to be in consistent with observations, the scale radius of the halo has been fixed to 12 kpc,

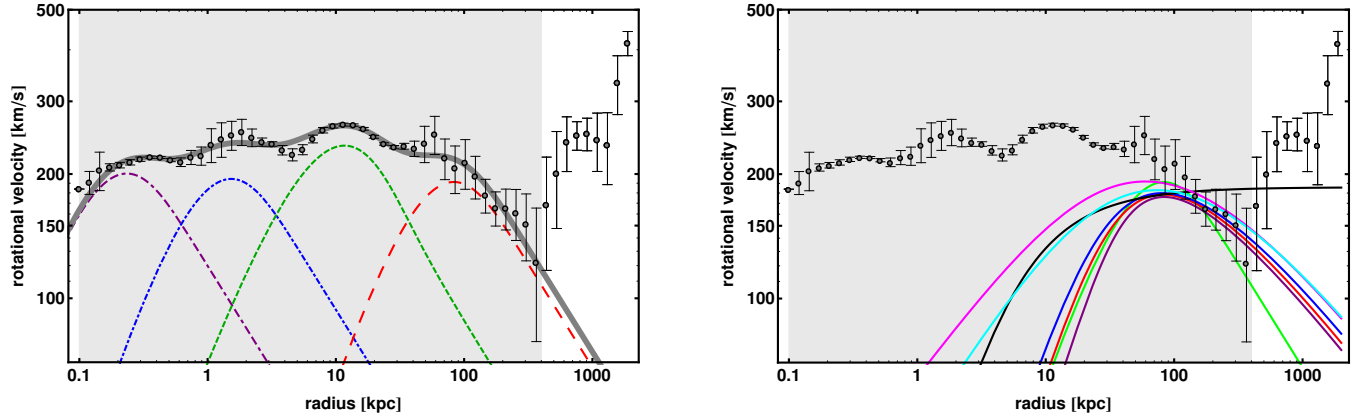


Figure 3. Reconstructed RC of M31. Like in Fig. 2, the shaded area marks the data (black dots with error bars) considered for the fitting. Left panel: best-fit total RC (thick, gray) composed of inner bulge (ES, dash-dash-dotted purple), main bulge (ES, dot-dashed blue), disk (Freeman, dashed green) and halo (ES, long-dashed red) curves. Right panel: RC of the halo of M31 with ISO (black), Burkert (blue), Beta (red), Moore (magenta), ES (green), NFW (cyan) and Brownstein (purple) profiles, obtained from the fitting with inner and main bulges (see Table 2).

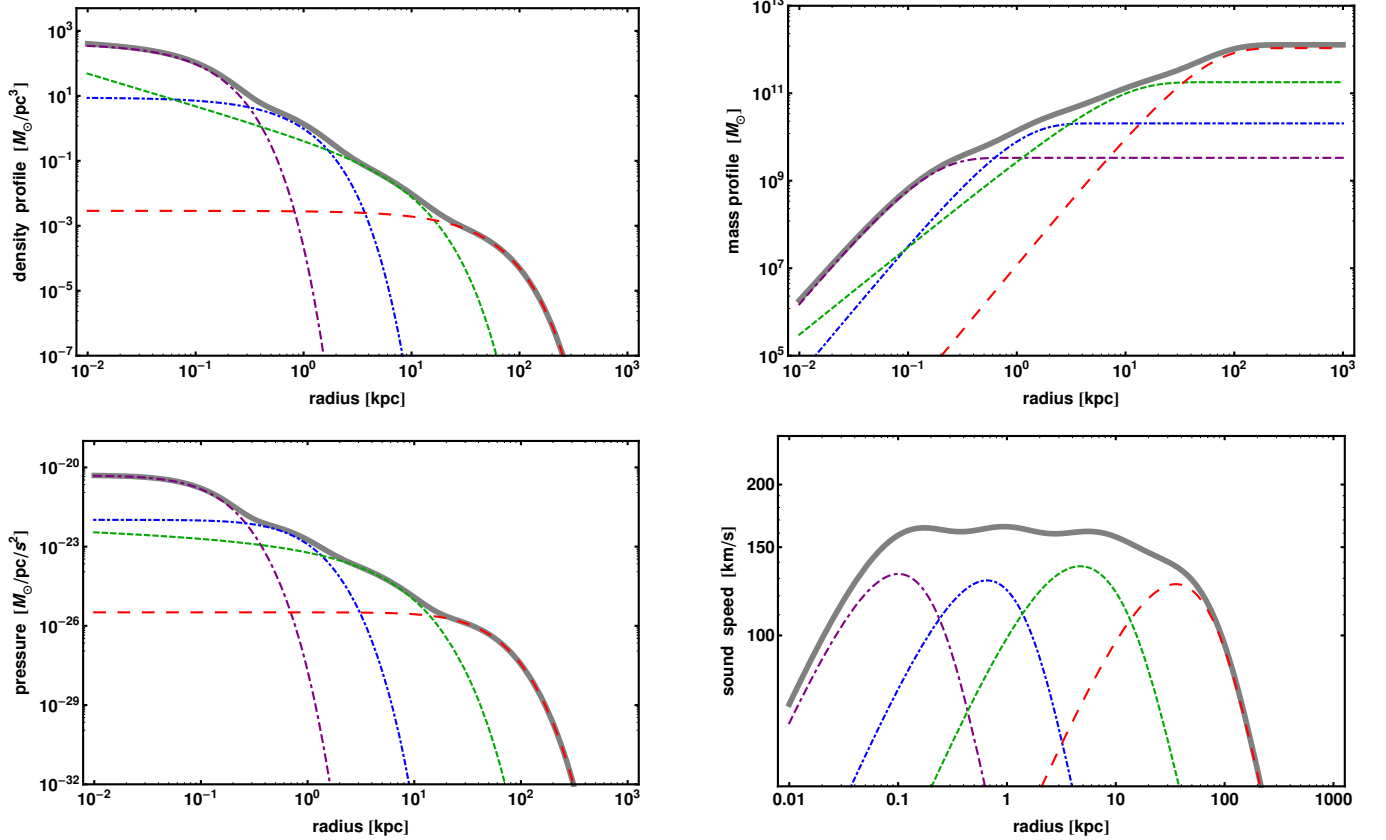


Figure 4. Density (top left), mass (top right), pressure (bottom left) and speed of sound (bottom right) profiles of M31 for the best-fit combination of models (see Table 3). The net profiles and the curves for inner and main bulges, disk and DM halo have the same symbols and colors of the left panel of Fig. 3.

which substantially facilitated the analyses. However, here we leave free the scale radius and infer it from the fit, which we presume is more reasonable than fixing it in advance.

Table 5 lists the best-fit results obtained from the ~ 0.1 –400 kpc RC by considering a single bulge Sofue (2015). Like for the case of M31, we here fixed the de Vaucouleurs profile for the bulge, the Freeman profile for the disk, whereas for the halo we explored the

profiles in Eqs. (1)–(6) and the ES profile. Again, the last combination of models listed in Table 5 represents a direct comparison, though performed with a different methodology (see Sec. 3), with the results of Sofue (2015) summarized Table 4.

Table 6 lists the best-fit results obtained from the ~ 0.01 –400 kpc RC data by splitting the bulge into inner and main components in analogy to Sofue (2013). We fixed the exponential sphere density

Table 4. The best-fit parameters of the MW from Sofue (2015). The halo model is the NFW profile and its mass has been calculated within $r = 200$ kpc.

| Parts | Total mass ($10^{11} M_{\odot}$) | Scale radius (kpc) | Central density ($10^{-3} M_{\odot}/\text{pc}^3$) |
|-------|---------------------------------------|-----------------------|--|
| Bulge | 0.25 ± 0.02 | 0.87 ± 0.07 | — |
| Disk | 1.12 ± 0.40 | 5.73 ± 1.23 | — |
| Halo | 5.7 ± 5.1 | 10.7 ± 2.9 | 18.2 ± 7.4 |

profile for both inner and main bulges and the Freeman density profile for the disk, whereas for the halo we explored all the DM density profiles in Eqs. (1)–(6) and the exponential sphere profile.

The comparison between the results of Tables 5–6 is not straightforward. The reason is that to reproduce the results of Sofue (2015) summarized in Table 4 and to perform the analysis shown in Table 5, the fits of the one bulge cases focused on the range ~ 0.1 –400 kpc, whereas the fits of the two bulge cases focused on the range ~ 0.01 –400 kpc to perform better modeling of the inner bulge. However, taking in mind the above caveat, we performed the BIC tests for both cases and computed the difference ΔBIC with respect to the model providing the lowest value BIC_0 . According to this test, it turned out that the models with ES density profiles for both inner and main bulges indeed fit better than the de Vaucouleurs profile for a single bulge, with the latter models providing $\Delta\text{BIC} \gtrsim 100$ with respect to the former ones. In particular, in Table 6 we see that the best-fit model with the lowest value $\text{BIC}_0 = 134.16$ is the two-bulge model with a DM halo described by the ES density profile. The NFW profile, like the Moore profile, does not perform well, since $\Delta\text{BIC} \approx 16$. In absolute, the worst fit is given by the ISO profile with $\Delta\text{BIC} \approx 58$, as certified by the fact that the RC of the MW is not flat in the halo region (see Figure 5).

Also among the fits with a single bulge described by the de Vaucouleurs profile (strongly excluded with respect to the fits with inner and main bulges), the DM ES profile ($\Delta\text{BIC} \approx 160$) and Brownstein profile ($\Delta\text{BIC} \approx 166$) fit better than NFW profile ($\Delta\text{BIC} \gtrsim 191$), whereas the ISO profile ($\Delta\text{BIC} \approx 197$) is definitely the worst-performing one (see Table 5).

Finally, fits with two de Vaucouleurs profiles for inner and main bulges lead to higher BIC and ΔBIC values. Again, these analyses have not been shown here to keep the presentation clear and simple.

The left panel of Fig. 6 portrays the RC data with error bars of the MW galaxy with the best-fitting curve composed of the inner and main bulges modeled with two ES profiles, the disk with the Freeman profile, and the halo region with the ES model (see values in Table 6). The right panel of Fig. 6 displays the halo RC part with the DM profiles considered in this work (see the values in Table 6).

Fig. 7 displays the density $\rho(r)$ (top left panel), the mass $M(r)$ (top right panel), the pressure $P(r)$ (bottom left panel) and the speed of sound c_s (bottom right panel) radial distributions obtained from the combination of models best-fitting the RC of the MW (see Fig. 6 and Table 6). Similar results have been obtained for the MW in Boshkayev et al. (2021).

5 FINAL OUTLOOKS AND PERSPECTIVES

In this work, the rotation curve of the Andromeda galaxy was analyzed from the galactic center to the halo region. Following Sofue (2013), the exponential sphere profile was involved in describing the observational data in the bulge and disk of the galaxy. Moreover, the bulge was decomposed into inner and main parts in analogy to Sofue (2013), where the same approach was applied to the Milky Way

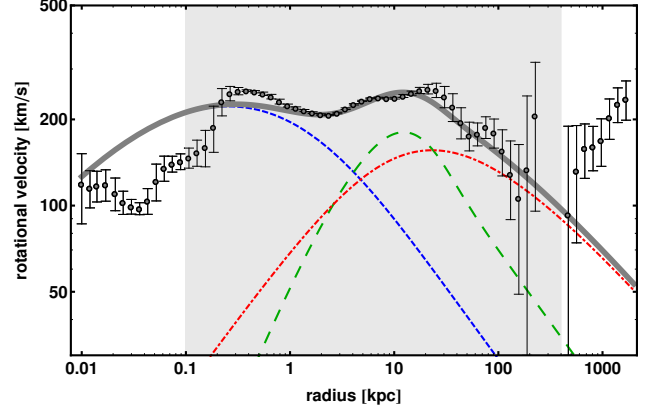


Figure 5. Best-fit RC of the MW (thick, gray) composed of bulge (de Vaucouleurs, dot-dashed blue), disk (Freeman, dashed green) and halo (NFW, long-dashed red) components. The shaded area marks the data (black dots with error bars) considered for the fitting. Reproduced from Sofue (2015).

galaxy. The NFW, Burkert, Moore, Isothermal, Beta and Brownstein along with the exponential density profiles were used in the halo region to analyze the rotation curve for the Andromeda Galaxy.

The Bayesian information criterion (BIC) (Yunis et al. 2020) was used to find the model that showed the best results for a given galaxy out of six models. Among all of the models the exponential density and Brownstein profiles showed good results for the Andromeda galaxy in the halo region. The exponential sphere profile was better for the bulge with respect to the de Vaucouleurs model.

Table 1, which we retrieved from Sofue (2015), is a reference and starting point for our analyses. Knowing what we approximately expect to obtain, we extended the results of Table 1 in Table 2 showing that the NFW profile is good, but not the best profile among the existing alternatives. Furthermore, we continued our analyses in Table 3. Following Sofue (2015), the bulge was decomposed into inner and main components modelling them with the exponential density profiles.

It should be stressed that one is free to consider various sets of combinations (permutations) of the models within the galaxy. However, for most of them the BIC values were large. Therefore, they have been omitted. Wherever we involve the de Vaucouleurs profile, the BIC was high. As soon as we abandoned the de Vaucouleurs profile and used the exponential density profile, the BIC started decreasing, see Table 3 for details.

According Peñarrubia et al. (2014) the median mass of the Andromeda galaxy, including the dark matter mass, is around $(1.5 \pm 0.5) \times 10^{12} M_{\odot}$. Chapman et al. (2006) using NFW profile in their analyses, indicate the size of the Andromeda galaxy to be ~ 70 kpc in diameter, so ~ 35 kpc in radius. These data can be used as additional references for our findings. Thus, the results obtained in Table 3 for the Brownstein and NFW profiles are consistent with the ones in the literature. However, from the statistical point of view the exponential density profile turned out to be the best.

Using updated data points for the RC given by Sofue (2015), similar analyses have been carried out also for the Milky Way galaxy. Here, the two bulges model with the exponential sphere profile was better than a single bulge model with the de Vaucouleurs profile. For the halo region, the exponential sphere profile again provides statistically the best fit.

In Table 7, we show the best fit parameters for the two galaxies. It turned out that the Milky Way is roughly twice less massive than the

Table 5. Best-fit RC parameters of the MW obtained by considering one bulge (de Vaucouleurs), disk (Freeman) and the halo models considered in this work. The halo mass has been calculated within $r = 200$ kpc. The ΔBIC value is computed with respect to the minimum BIC in Table 6.

| Bulge | | Disk | | Halo | | | ΔBIC |
|--------------------------------|------------------------|--------------------------------|------------------------|---|-------------------------|--------------------------------|--------------------|
| M_b ($10^{11} M_\odot$) | r_b (kpc) | M_d ($10^{11} M_\odot$) | r_d (kpc) | ρ_0 ($10^{-3} M_\odot/\text{pc}^3$) | r_0 (kpc) | M_h ($10^{11} M_\odot$) | |
| de Vaucouleurs | | Freeman | | Beta | | | 172.57 |
| $0.20^{+0.01}_{-0.01}$ | $0.49^{+0.03}_{-0.03}$ | $0.75^{+0.09}_{-0.07}$ | $3.38^{+0.19}_{-0.17}$ | $15.02^{+3.74}_{-3.72}$ | $12.82^{+1.89}_{-1.43}$ | $9.72^{+4.43}_{-3.70}$ | |
| de Vaucouleurs | | Freeman | | Brownstein | | | 165.56 |
| $0.20^{+0.01}_{-0.01}$ | $0.49^{+0.02}_{-0.02}$ | $0.89^{+0.06}_{-0.04}$ | $3.61^{+0.14}_{-0.12}$ | $7.84^{+0.83}_{-1.24}$ | $15.45^{+1.40}_{-0.67}$ | $9.32^{+2.41}_{-1.81}$ | |
| de Vaucouleurs | | Freeman | | Burkert | | | 172.53 |
| $0.20^{+0.01}_{-0.01}$ | $0.50^{+0.01}_{-0.04}$ | $0.50^{+0.15}_{-0.02}$ | $2.95^{+0.29}_{-0.09}$ | $47.65^{+1.85}_{-19.39}$ | $8.55^{+2.35}_{-0.15}$ | $9.02^{+6.45}_{-3.69}$ | |
| de Vaucouleurs | | Freeman | | ES | | | 160.30 |
| $0.20^{+0.01}_{-0.01}$ | $0.48^{+0.02}_{-0.03}$ | $0.74^{+0.06}_{-0.05}$ | $3.37^{+0.14}_{-0.12}$ | $20.33^{+3.03}_{-3.03}$ | $9.97^{+0.80}_{-0.60}$ | $5.07^{+1.43}_{-1.18}$ | |
| de Vaucouleurs | | Freeman | | ISO | | | 197.73 |
| $0.21^{+0.01}_{-0.01}$ | $0.53^{+0.03}_{-0.02}$ | $0.80^{+0.03}_{-0.02}$ | $3.62^{+0.12}_{-0.07}$ | $19.30^{+0.68}_{-1.59}$ | $6.81^{+0.24}_{-0.41}$ | $21.30^{+1.66}_{-3.07}$ | |
| de Vaucouleurs | | Freeman | | Moore | | | 196.29 |
| $0.18^{+0.01}_{-0.01}$ | $0.43^{+0.03}_{-0.02}$ | $0.67^{+0.07}_{-0.07}$ | $3.89^{+0.13}_{-0.11}$ | $4.33^{+1.71}_{-0.86}$ | $25.22^{+3.11}_{-3.49}$ | $12.15^{+6.02}_{-4.73}$ | |
| de Vaucouleurs | | Freeman | | NFW | | | 191.10 |
| $0.18^{+0.01}_{-0.01}$ | $0.44^{+0.03}_{-0.03}$ | $0.62^{+0.09}_{-0.08}$ | $3.77^{+0.11}_{-0.20}$ | $9.73^{+2.70}_{-3.68}$ | $18.05^{+5.31}_{-1.94}$ | $12.00^{+8.78}_{-5.23}$ | |

Table 6. Best-fit RC parameters of the MW obtained by considering inner (ES) and main bulges (ES), disk (Freeman) and the halo models considered in this work. The halo mass has been calculated within $r = 200$ kpc. The ΔBIC value is computed with respect to the model with the ES DM halo.

| Inner Bulge | | Main Bulge | | Disk | | Halo | | | ΔBIC |
|-----------------------------------|-------------------------------|-----------------------------------|---------------------------|--------------------------------|------------------------|---|-------------------------|--------------------------------|--------------------|
| M_{ib} ($10^{11} M_\odot$) | r_{ib} (kpc) | M_{mb} ($10^{11} M_\odot$) | r_{mb} (kpc) | M_d ($10^{11} M_\odot$) | r_d (kpc) | ρ_0 ($10^{-3} M_\odot/\text{pc}^3$) | r_0 (kpc) | M_h ($10^{11} M_\odot$) | |
| ES | | ES | | Freeman | | Beta | | | 12.59 |
| $0.00056^{+0.00006}_{-0.00003}$ | $0.0034^{+0.0009}_{-0.0006}$ | $0.094^{+0.001}_{-0.001}$ | $0.130^{+0.002}_{-0.002}$ | $0.48^{+0.08}_{-0.03}$ | $2.41^{+0.18}_{-0.06}$ | $33.24^{+4.53}_{-8.83}$ | $9.33^{+1.69}_{-0.57}$ | $9.37^{+4.67}_{-2.91}$ | |
| ES | | ES | | Freeman | | Brownstein | | | 8.82 |
| $0.00059^{+0.00003}_{-0.00005}$ | $0.0040^{+0.0004}_{-0.0009}$ | $0.096^{+0.001}_{-0.002}$ | $0.132^{+0.001}_{-0.003}$ | $0.68^{+0.02}_{-0.06}$ | $2.82^{+0.05}_{-0.13}$ | $13.28^{+3.00}_{-0.70}$ | $12.82^{+0.34}_{-1.40}$ | $9.66^{+2.28}_{-2.82}$ | |
| ES | | ES | | Freeman | | Burkert | | | 14.49 |
| $0.00058^{+0.00004}_{-0.00004}$ | $0.00380^{+0.0005}_{-0.0008}$ | $0.094^{+0.002}_{-0.001}$ | $0.130^{+0.003}_{-0.002}$ | $0.47^{+0.02}_{-0.02}$ | $2.43^{+0.05}_{-0.05}$ | $47.65^{+2.20}_{-3.66}$ | $9.12^{+0.34}_{-0.21}$ | $10.67^{+1.14}_{-1.04}$ | |
| ES | | ES | | Freeman | | ES | | | 0.00 |
| $0.00059^{+0.00005}_{-0.00004}$ | $0.0039^{+0.0004}_{-0.0010}$ | $0.096^{+0.001}_{-0.003}$ | $0.132^{+0.001}_{-0.003}$ | $0.59^{+0.02}_{-0.04}$ | $2.68^{+0.04}_{-0.13}$ | $30.37^{+4.33}_{-2.76}$ | $8.69^{+0.47}_{-0.54}$ | $5.01^{+1.09}_{-1.04}$ | |
| ES | | ES | | Freeman | | ISO | | | 58.22 |
| $0.00063^{+0.00002}_{-0.00010}$ | $0.0043^{+0.0005}_{-0.0011}$ | $0.098^{+0.00}_{-0.001}$ | $0.133^{+0.001}_{-0.002}$ | $0.44^{+0.01}_{-0.01}$ | $2.47^{+0.01}_{-0.05}$ | $57.04^{+2.45}_{-0.53}$ | $4.50^{+0.03}_{-0.15}$ | $28.04^{+1.26}_{-1.81}$ | |
| ES | | ES | | Freeman | | Moore | | | 17.72 |
| $0.00052^{+0.00003}_{-0.00006}$ | $0.0027^{+0.0012}_{-0.0001}$ | $0.083^{+0.001}_{-0.003}$ | $0.122^{+0.001}_{-0.004}$ | $0.28^{+0.05}_{-0.05}$ | $3.03^{+0.02}_{-0.14}$ | $20.35^{+3.87}_{-3.50}$ | $13.16^{+1.02}_{-0.88}$ | $11.35^{+3.1}_{-2.74}$ | |
| ES | | ES | | Freeman | | NFW | | | 16.31 |
| $0.00056^{+0.00001}_{-0.00008}$ | $0.0036^{+0.0003}_{-0.0011}$ | $0.087^{+0.001}_{-0.004}$ | $0.124^{+0.002}_{-0.004}$ | $0.29^{+0.01}_{-0.09}$ | $2.79^{+0.06}_{-0.16}$ | $30.20^{+13.33}_{-2.57}$ | $11.49^{+0.53}_{-1.75}$ | $11.31^{+5.17}_{-4.50}$ | |

Andromeda galaxy. These results have been compared with those given in Table 2 of Ref. Sofue (2015) and in Table 6 of Ref. Sofue (2017). It appeared that the order of the parameters are in agreement with Sofue (2015) and Sofue (2017). The slight differences are due to different approaches employed to fit the data and models chosen for the galaxy halos. As one can see from the Tables, the halo profile affects the inner parts of the galaxies. Therefore, the scale radius, characteristic densities and, as a consequences, the mass vary from the ones reported in the literature.

For both galaxies, we investigated the role of the sound speed as it is closely linked to perturbation theory and structure formation. In particular, it determines the length above which gravitational instability overcomes the radiation pressure, where perturbations can significantly grow. The two galaxies exhibit similar behaviors with different shapes of the rotation curves; this is probably due to the fact that the two galaxies, albeit similar, are morphologically different.

Though one can determine the distribution of dark matter mass in galaxies with the help of rotation curves by assuming various the-

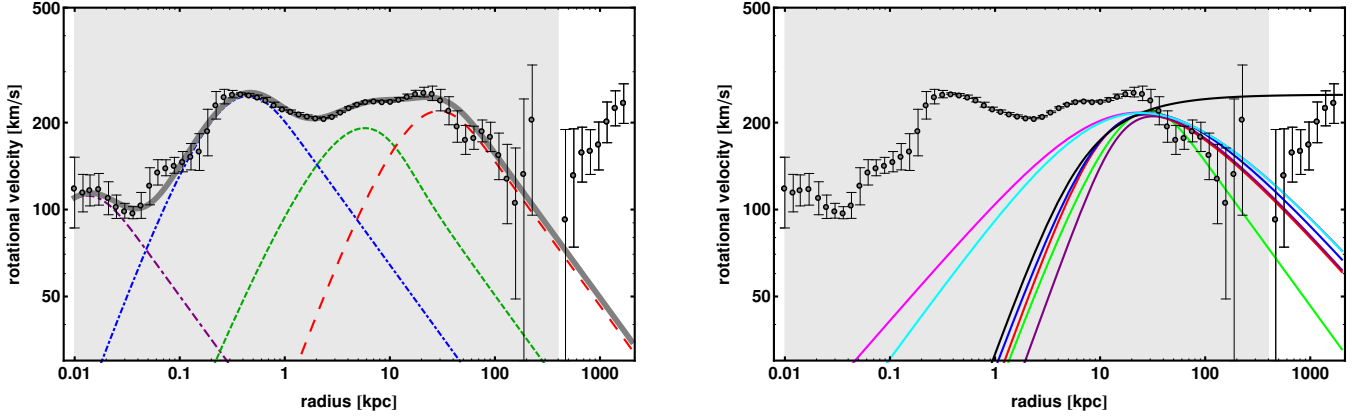


Figure 6. Reconstructed RC of the MW. Left panel: best-fit total RC composed of inner and main bulges, disk and ES profile for the halo. Right panel: RC of the halo of the MW with Beta, Brownstein, Burkert, ES, ISO, Moore and NFW profiles. The net profiles and the curves for inner and main bulges, disk and DM halo have the same symbols and colors of the left panel of Fig. 3. The best-fit values are taken from Table 6.

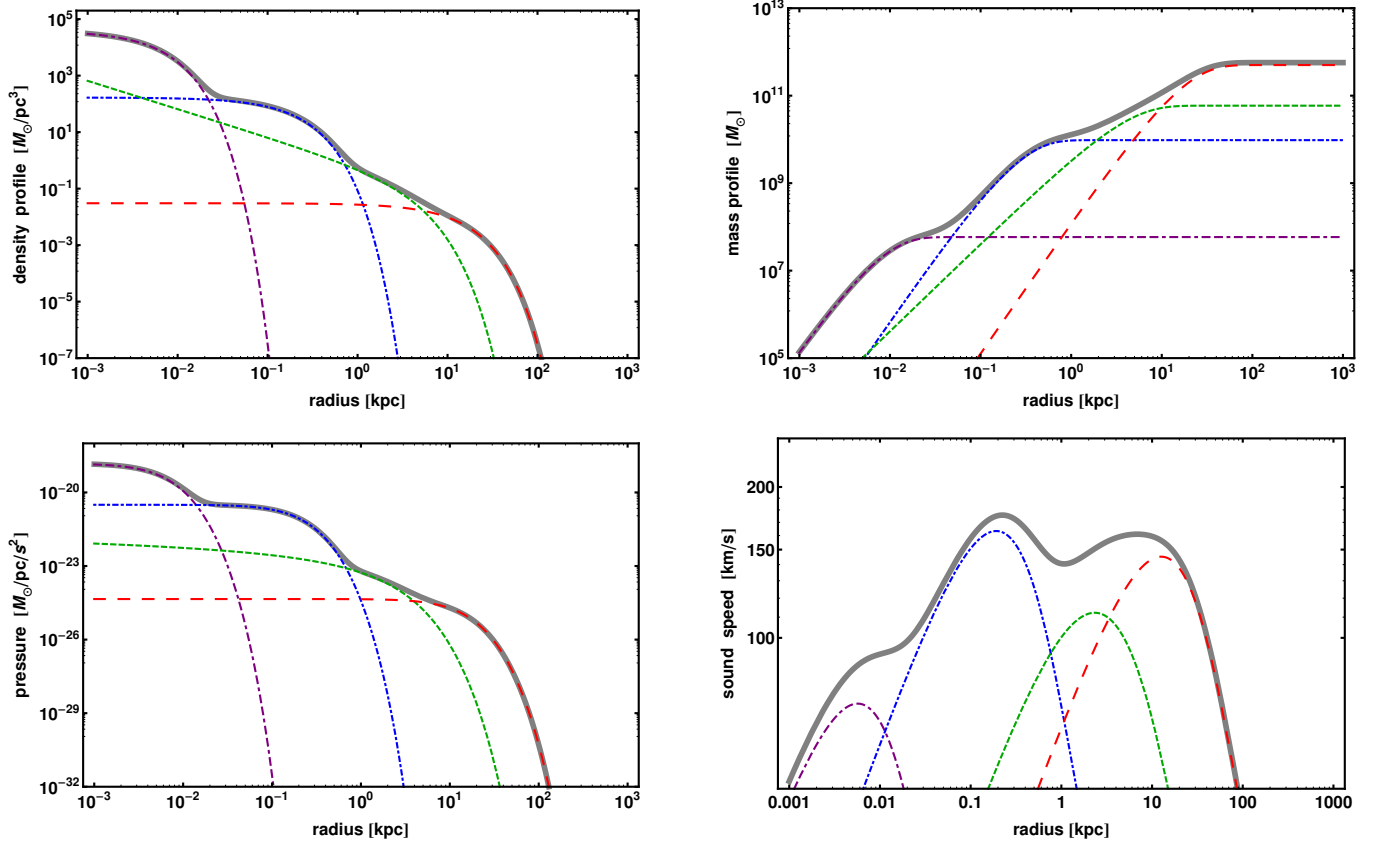


Figure 7. Density (top left), mass (top right), pressure (bottom left) and speed of sound (bottom right) profiles of the MW for the best-fit combination of models (see Table 6). The net profiles and the curves for inner and main bulges, disk and DM halo have the same symbols and colors of the left panel of Fig. 6.

oretical models, it is not yet clear why dark matter is distributed differently in every galaxy and what is its role in the evolution of the universe. The realization that the nature of the main matter content of the Universe is not well-understood, is a solid motivation to study its properties in future works.

ACKNOWLEDGEMENTS

OL expresses is grateful to the Department of Physics of the Al-Farabi University for hospitality during the period in which this manuscript has been written. This research has been partially funded by the Science Committee of the Ministry of Science and Higher Education of the Republic of Kazakhstan (Grant No. AP08052311). The work of HQ was partially supported by PAPIIT-DGAPA-

Table 7. Comparison of the best-fit parameters for M31 and the MW.

| Component | Parameter | M31 | Milky Way |
|-------------|--|---------------------------|---------------------------------|
| Inner bulge | r_{ib} (kpc) | $0.069^{+0.003}_{-0.003}$ | $0.0039^{+0.0004}_{-0.0010}$ |
| | M_{ib} ($10^{11} M_{\odot}$) | $0.033^{+0.002}_{-0.002}$ | $0.00059^{+0.00005}_{-0.00004}$ |
| Main bulge | r_{mb} (kpc) | $0.45^{+0.02}_{-0.03}$ | $0.132^{+0.001}_{-0.003}$ |
| | M_{mb} ($10^{11} M_{\odot}$) | $0.20^{+0.01}_{-0.02}$ | $0.096^{+0.001}_{-0.003}$ |
| Disk | r_d (kpc) | $5.43^{+0.05}_{-0.23}$ | $2.68^{+0.04}_{-0.13}$ |
| | M_d ($10^{11} M_{\odot}$) | $1.79^{+0.03}_{-0.08}$ | $0.59^{+0.02}_{-0.04}$ |
| Halo | r_0 (kpc) | $24.59^{+1.40}_{-1.00}$ | $8.69^{+0.47}_{-0.54}$ |
| | ρ_0 ($10^{-3} M_{\odot}/\text{pc}^3$) | $2.88^{+0.41}_{-0.26}$ | $30.37^{+4.33}_{-2.76}$ |
| | M_h ($10^{11} M_{\odot}$) | $10.64^{+2.34}_{-1.59}$ | $5.01^{+1.09}_{-1.04}$ |
| Total mass | M_{tot} ($10^{11} M_{\odot}$) | $12.67^{+2.34}_{-1.59}$ | $5.70^{+1.09}_{-1.04}$ |

UNAM, Grant No. 114520, and Conacyt-Mexico, Grant No. A1-S-31269.

REFERENCES

Arjona R., Cardona W., Nesseris S., 2019, *Phys. Rev. D*, **99**, 043516

Bai Y., Long A. J., Lu S., 2020, *J.C.A.P.*, **2020**, 044

Banik I., Thies I., Famaey B., Candlish G., Kroupa P., Ibata R., 2020, *Astrophys. J.*, **905**, 135

Barranco J., Bernal A., Núñez D., 2015, *Mon. Not. Roy. Astr. Soc.*, **449**, 403

Beaton R. L., et al., 2007, *Astrophys. J. Lett.*, **658**, L91

Belfiglio A., Luongo O., Mancini S., 2022, *Phys. Rev. D*, **105**, 123523

Bernal T., Fernández-Hernández L. M., Matos T., Rodríguez-Meza M. A., 2018, *Mon. Not. Roy. Astr. Soc.*, **475**, 1447

Bernardeau F., Colombi S., Gaztanaga E., Scoccimarro R., 2002, *Phys. Rept.*, **367**, 1

Bertone G., Hooper D., 2018, *Reviews of Modern Physics*, **90**, 045002

Bertone G., Hooper D., Silk J., 2005, *Phys. Rep.*, **405**, 279

Binney J., Tremaine S., 1987, *Galactic dynamics*. Princeton, N.J.: Princeton University Press

Blaña Díaz M., Wegg C., Gerhard O., Erwin P., Portail M., Opitsch M., Saglia R., Bender R., 2017, *Mon. Not. Roy. Astr. Soc.*, **466**, 4279

Boshkayev K., D’Agostino R., Luongo O., 2019, *Eur. Phys. J. C*, **79**, 332

Boshkayev K., Konysbayev T., Kurmanov E., Luongo O., Malafarina D., Mutalipova K., Zhumakhanova G., 2021, *Mon. Not. Roy. Astr. Soc.*, **508**, 1543

Bosma A., 1981, *AJ*, **86**, 1791

Brandt T. D., 2016, *Astrophys. J. Lett.*, **824**, L31

Brownstein J. R., Moffat J. W., 2006, *The Astrophysical Journal*, **636**, 721

Burkert A., 1995, *The Astrophysical Journal Letters*, **447**, L25

Capozziello S., D’Agostino R., Luongo O., 2019, *Int. J. Mod. Phys. D*, **28**, 1930016

Carignan C., Chemin L., Huchtmeier W. K., Lockman F. J., 2006, *Astrophys. J. Lett.*, **641**, L109

Chapline G. F., Frampton P. H., 2016, *J.C.A.P.*, **2016**, 042

Chapman S. C., Ibata R., Lewis G. F., Ferguson A. M. N., Irwin M., McConnachie A., Tanvir N., 2006, *Astrophys. J.*, **653**, 255

Corbelli E., Lorenzoni S., Walterbos R., Braun R., Thilker D., 2010, *Astron. Astrophys.*, **511**, A89

Dehghani R., Salucci P., Ghaffarnejad H., 2020, *Astron. Astrophys.*, **643**, A161

Elson E. C., 2014, *Mon. Not. Roy. Astr. Soc.*, **437**, 3736

Event Horizon Telescope Collaboration et al., 2019, *Astrophys. J. Lett.*, **875**, L4

Faber S. M., Gallagher J. S., 1979, *Annual Rev. of Astron. Astrophys.*, **17**, 135

Freeman K. C., 1970, *Astrophys. J.*, **160**, 811

Herrera G., Ibarra A., 2021, *Physics Letters B*, **820**, 136551

Jimenez R., Verde L., Oh S. P., 2003, *Monthly Notices of the Royal Astronomical Society*, **339**, 243

Katz A., Kopp J., Sibiryakov S., Xue W., 2020, *Mon. Not. Roy. Astr. Soc.*, **496**, 564

Marrodán Undagoitia T., Rodejohann W., Wolf T., Yaguna C. E., 2022, *Progress of Theoretical and Experimental Physics*, **2022**, 013F01

Milgrom M., 2020, *Stud. Hist. Phil. Sci. B*, **71**, 170

Moore B., Governato F., Quinn T., Stadel J., Lake G., 1998, *Astrophys. J. Lett.*, **499**, L5

Mould J., 2013, *Publ. Astron. Soc. Australia*, **30**, e027

Nakama T., 2020, *Physics of the Dark Universe*, **28**, 100476

Navarro J. F., Frenk C. S., White S. D. M., 1995, *MNRAS*, **275**, 720

Navarro J. F., Frenk C. S., White S. D. M., 1996, *Astrophys. J.*, **462**, 563

Peñarrubia J., Ma Y.-Z., Walker M. G., McConnachie A., 2014, *Mon. Not. Roy. Astr. Soc.*, **443**, 2204

Quiskamp A. P., McAllister B. T., Altin P., Ivanov E. N., Goryachev M., Tobar M. E., 2022, arXiv e-prints, p. arXiv:2203.12152

Roberts M. S., 1978, *AJ*, **83**, 1026

Rubin V. C., Ford W. Kent J., 1970, *Astrophys. J.*, **159**, 379

Rubin V. C., Ford W. K. J., Thonnard N., 1980, *Astrophys. J.*, **238**, 471

Salucci P., 2019a, *Astron. Astrophys. Rev.*, **27**, 2

Salucci P., 2019b, *Astron. Astrophys. Rev.*, **27**, 2

Sofue Y., 2009, *Publ. Astr. Soc. Japan*, **61**, 153

Sofue Y., 2013, *Publications of the Astronomical Society of Japan*, **65**, 118

Sofue Y., 2015, *Publ. Astr. Soc. Japan*, **67**, 75

Sofue Y., 2017, *Publ. Astr. Soc. Japan*, **69**, R1

Sofue Y., 2020, *Galaxies*, **8**, 37

Woithe J., Kersting M., 2021, *Physics Education*, **56**, 035011

Yang Y., 2022, *Phys. Rev. D*, **106**, 043516

Yunis R., Argüelles C. R., Mavromatos N. E., Moliné A., Krut A., Carinci M., Rueda J. A., Ruffini R., 2020, *Physics of the Dark Universe*, **30**, 100699

de Vaucouleurs G., 1958, *Astrophys. J.*, **128**, 465